Nonlinear Viscosity Law in Finite-Element Analysis of High Damping Rubber Bearings and Expansion Joints

A. F. M. S. Amin[1]; A. R. Bhuiyan[2]; T. Hossain[3]; and Y. Okui[4]

Abstract: A simple computational strategy for finite-element implementation of a finite-strain viscohyperelasticity model for rubber-like materials was developed. The constitutive model has had a strong physical significance because of the explicit consideration of the nonlinear dependence of viscosity through internal variables (e.g., past maximum overstress and current deformation). To simulate the stress-strain response for particular one-dimensional boundary value problems, a scheme for solving the first-order differential equation representing the viscosity-induced strain-rate effect of rubber was proposed. The scheme was successful in reproducing experimental results obtained from high-damping rubber specimens. In addition, the wider applicability of the proposed strategy in simulation was tested by verifying the numerical results with independent experiments on full-scale high-damping rubber bearings with different geometries and loading rates. The effect of shape factor on bearing responses was examined through numerical examples obtained from different finite-element models subjected to the same load and loading rate. Finally, the proposed computational strategy was applied to locate the regions of stress concentrations in steel plate laminated rubber expansion joints used widely to transfer reactions at central-hinge locations on balanced cantilever highway bridges. **DOI: 10.1061/(ASCE)EM.1943-7889.0000888.** *© 2014 American Society of Civil Engineers.*

Author keywords: High damping rubber; Nonlinear viscosity law; Finite-element implementation; Isolation bearing; Expansion joints.

Introduction

General

The use of laminated rubber bearings for seismic isolation in reducing earthquake-induced damages is widely recognized (Kelly 1997). Vulcanized natural rubber or high-damping rubber is commonly used with alternate layers of steel plates [Fig. 1(c)] to fabricate such bearings. The steel plates placed in horizontal layers provide vertical stiffness to resist a superimposed dead load but, at the same time, ensure the low horizontal shear stiffness of the device. The horizontal flexibility offered thus by the device is important in resisting lateral loads caused by earthquakes. In addition, steel plate laminated rubber expansion joints (Figs. 2 and 3) are often used at the central hinge locations of balanced cantilever bridges (Spuler et al. 2010). In such arrangements, the expansion joints generally used to accommodate temperature-induced bridge seating displacements also transfer the vertical reaction forces arising from the moving loads to the adjacent spans in service conditions. Two approaches are followed in the industry to design and shape these devices. The first approach relies on data obtained from testing the prototype devices, whereas the other approach follows a rigorous numerical procedure [e.g., the FEM] that considers geometric and material nonlinearities.

[1]Professor, Dept. of Civil Engineering, Bangladesh Univ. of Engineering and Technology, Dhaka 1000, Bangladesh (corresponding author). E-mail: samin@ce.buet.ac.bd

[2]Professor, Dept. of Civil Engineering, Chittagong Univ. of Engineering and Technology, Chittagong 4349, Bangladesh.

[3]Lecturer, Dept. of Civil Engineering, Dhaka Univ. of Engineering and Technology, Gazipur 1700, Bangladesh.

[4]Professor, Dept. of Civil and Environmental Engineering, Saitama Univ., 255 Shimo Okubo, Sakura-ku, Saitama 338-8570, Japan.

Note. This manuscript was submitted on December 20, 2011; approved on September 30, 2014; published online on November 3, 2014. Discussion period open until April 3, 2015; separate discussions must be submitted for individual papers. This paper is part of the ***Journal of Engineering Mechanics***, © ASCE, ISSN 0733-9399/04014169(11)/$25.00.

Both approaches have their own limitations; however, the latter one offers better flexibility in making design iterations. Thus, sophistication in the development and implementation of an adequate material law to describe the pertinent mechanical behaviors of rubber-like materials is crucial.

Rate-Dependent Behavior in Rubber

The mechanical responses of rubbers depend strongly on loading history, current strain, and strain rate [see Amin et al. (2006a), Bergström and Boyce (1998), Lion (1996), and Miehe and Keck (2000) for state-of-the-art reviews.]. In high-damping rubber, these dependencies are strongly nonlinear (Amin 2001). The monotonic rate-independent response of rubber-like materials is generally reproduced by rate-independent hyperelasticity models (Mooney 1940; Rivlin and Saunders 1951; Treloar 1944). A detailed review of the historical development of different hyperelasticity models is presented elsewhere (Amin et al. 2002; Shariff 2000). To represent the viscosity-induced strain-rate effect, the total stress is usually decomposed into the equilibrium response and the overstress response. The total strain is decomposed into elastic and inelastic strains through multiplicative decomposition of the strain tensor (Lubliner 1973, 1985) (see Fig. 4 for the Zener model). The viscosity effect is reproduced by a relation between the overstress and the inelastic strain rate (Huber and Tsakmakis 2000). The equilibrium and instantaneous responses of the material are defined as the boundary state responses obtained from a specimen at infinitely slow and fast rates, respectively.

These two extreme responses define the boundary of a domain in which viscosity effects come into play. Multistep relaxation (MSR) tests and monotonic tests at fast rates are recognized as the standard tests for characterizing these elastic boundary states. Simple relaxation (SR) tests are used to characterize the viscosity phenomena that exist in between the two boundary states (Amin et al. 2002; Huber and Tsakmakis 2000). The difference between the current stress and the equilibrium stress is known as the overstress. Haupt and Sedlan (2001) assumed a nonlinear dependence of the viscosity on the current strain, whereas Amin et al. (2006b) proposed a general relationship

J. Eng. Mech., 2015, 141(6): 04014169

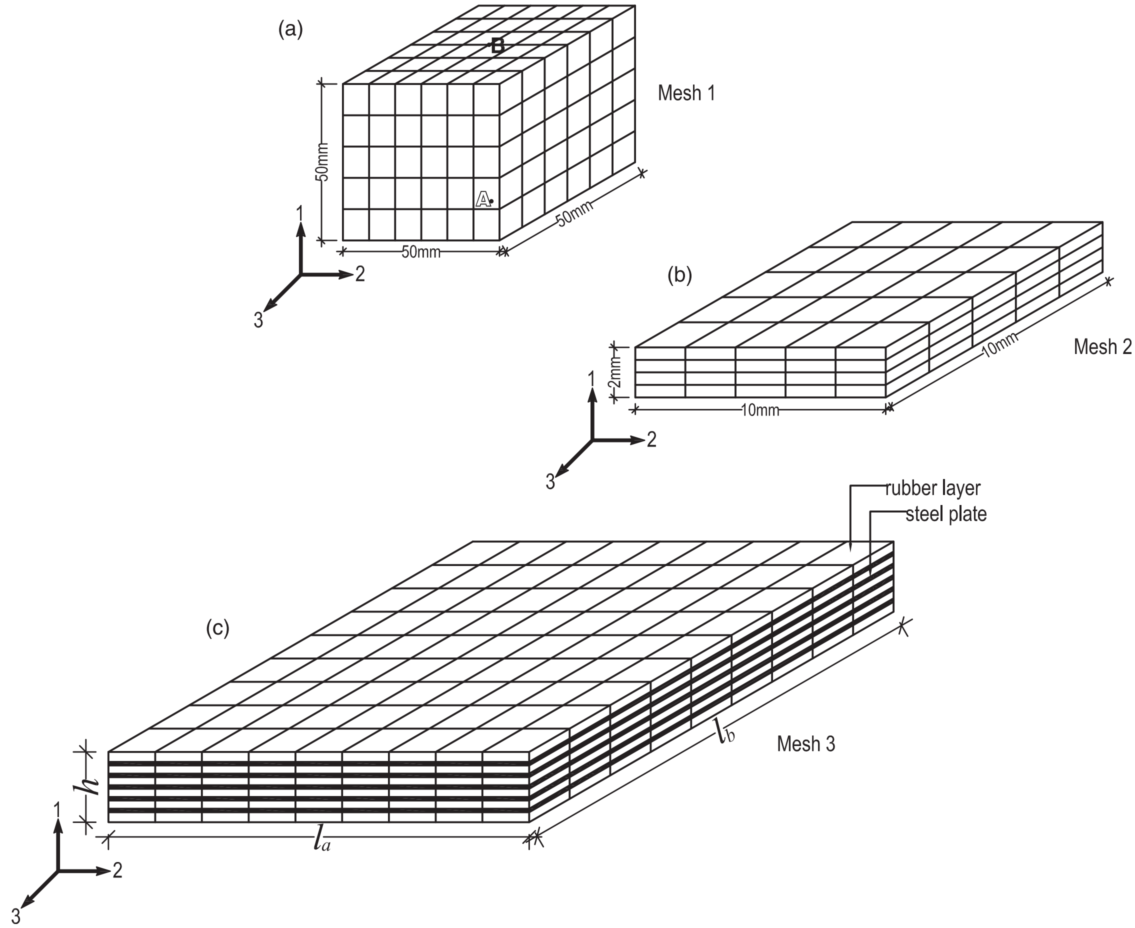

Fig. 1. FE mesh used for numerical simulation: (a) Mesh 1: uniaxial compression; boundary conditions: Node A at bottom surface (2-3 plane) is restrained in 1-, 2-, and 3-directions; all other nodes at bottom surface (2-3 plane) are free in 2-, 3-directions and restrained in 1-direction; Node B at top edge is restrained in 2- and 3-directions; all other nodes at top edge are free; displacement is applied along 1-direction; (b) Mesh 2: simple shear; boundary conditions: all nodes at the bottom edge (parallel to 2-3 plane) are restrained and fixed in 1-, 2-, and 3-directions; all nodes at the top edge (parallel to 2-3 plane) are restrained in 1- and 3-directions; displacement is applied along 2-direction; (c) Mesh 3: rubber bearing; boundary conditions: all nodes at the bottom edge (parallel to 2-3 plane) are restrained and fixed in 1-, 2,- and 3-directions; all nodes at the top edge (parallel to 2-3 plane) are restrained in 1- and 3-directions; displacement is applied along 2-direction; $h = n_r t_r + n_s t$; n_r = number of rubber layers; n_s = number of steel plates

Fig. 2. (Color) Replacement of rubber expansion joints of Japan-Bangladesh Friendship Bridge-I (23°31.858′N, 90°42.813′E) built in 1991 over the Meghna River, Bangladesh (images by A. F. M. S. Amin): (a) hinge points depict the location of expansion joints; (b) replacing the expansion joints as a part of bridge maintenance works

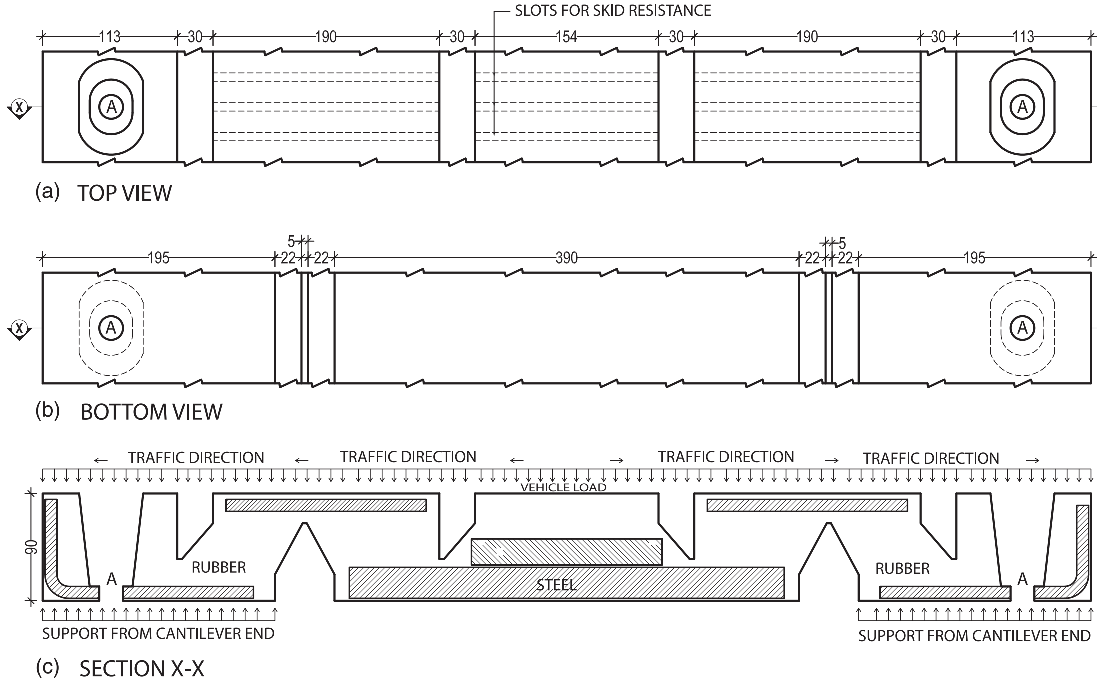

Fig. 3. As-built geometric details of the expansion joint of Japan-Bangladesh Friendship Bridge-I (23°31.858′N, 90°42.813′E) over the Meghna River, Bangladesh: (a) top view; (b) bottom view; (c) longitudinal sectional view (Section X-X)

between the overstress and the inelastic strain rate of both natural and high-damping rubber. Experimental evidence reported in these studies showed the strong dependence of the relation on past maximum overstress and current strain. The adequacy of the model in reproducing MSR, SR, and monotonic tests in compression and shear regimes was verified with experimental observations. Furthermore, the model was also successful in reproducing an independent set of test results at simple shear and uniaxial compression regimes with a unique set of parameters. More recently, Bhuiyan et al. (2009) identified a similar effect in high-damping rubber bearings and provided a thorough rheological characterization.

Numerical Treatment of Rate-Dependent Phenomena

The experimental identification and subsequent characterization of the phenomena are recognized to be the primary steps in developing a rational constitutive model and evaluating the parameters. However, the realization of benefits from such advancements for the design depends on successful implementation of the model in a finite-element (FE) procedure. In such a procedure, the nonlinear equations are solved in a linearized form to ascertain the stress field within the device (Simo et al. 1985; Simo 1987; Simo and Taylor 1991) by solving a boundary-value problem. Amin et al. (2006a) provided a state-of-the-art review on the FE analysis of rubber devices. As the primary step, they also implemented an improved hyperelasticity model into *FEAP 8.1*, which is a general-purpose open-source FE software (Taylor 2006) partially documented in Zienkiewicz and Taylor (2006). The capability of the improved hyperelasticity model in simulating rate-independent responses (e.g., equilibrium and elastic responses) was tested in that study by comparing experimental results in compression and shear regimes. Hasanpour and Ziaei-Rad (2008) presented a viscohyperelasticity model and the computational strategy for simulating the rate-dependent response of polymers at large strains. The model was adequate in reproducing the equilibrium and instantaneous responses but completely failed to represent the stress relaxation phenomenon.

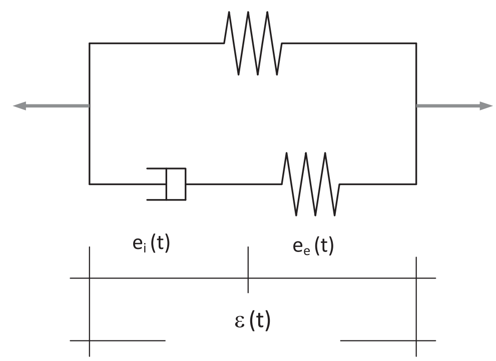

Fig. 4. Zener model

Nevertheless, simulation of relaxation phenomenon is one of the major attainable benchmarks in assessing the worthiness of a viscoelasticity model. In a later communication, Hasanpour et al. (2009) further discussed the difficulty of making an analytical calculation of the tangent modulus, which is an essential step in Newton's method. Dal and Kaliske (2009) presented a thorough numerical treatment to implement the Bergström and Boyce viscoelasticity model (Bergström and Boyce 1998) in a FE code. However, the model, which had a micromechanics-based inspiration, was found by the authors not to be applicable for general rate-dependent cases (e.g., simulation of devices using high-damping rubber). On the other hand, the fundamental promise demonstrated by the viscohyperelasticity model (Amin et al. 2006b) in analytical cases in describing the viscosity effect in high-damping rubber and natural rubber is yet to be explored in detail for solving boundary value problems in a FE technique. Nevertheless, the classical measurements presented there still motivate current researchers to develop and implement new models (Johlitz et al. 2007, 2008; Spathis and Kontou 2008).

Objectives and Methodology

The potential of the viscoelasticity model proposed in Amin et al. (2006b) motivated the authors to outline a computational strategy for FE analysis of rubber bearings and expansion joints. To maintain simplicity, the scope of the current work was restricted to the simulation of a specific one-dimensional problem. The match between the simulation results obtained using the proposed strategy on full-scale rubber bearings and the independent experiments was also checked. Finally, numerical experiments on rubber bearings with different shape factors and steel plate laminated rubber expansion joints were conducted to indicate the applicability of the proposed method to a wider area.

Constitutive Modeling

General Framework

A three-parameter Maxwell model (Zener model), as shown in Fig. 4, was used to model the rate-dependent behavior of rubber. The total stress was decomposed into two parts (i.e., the rate-independent equilibrium part and the rate-dependent overstress part). To model the rate-dependency phenomenon, the hyperelasticity models were required to be combined with the rate-dependent model. In this work, the improved hyperelasticity model proposed by Amin et al. (2006a) was combined with the rate-dependent model (Huber and Tsakmakis 2000) to formulate the total stress-strain relation. Eq. (1) represents the strain energy density function, W, expressed as a function of the invariants of the deformation tensor of an incompressible and isotropic elastic material

$$W(I_1, I_2) = C_5(I_1 - 3) + \frac{C_3}{N+1}(I_1 - 3)^N + \frac{C_4}{M+1}(I_1 - 3)^M + C_2(I_2 - 3) \quad (1)$$

where C_2, C_3, C_4, C_5, M, and N = material parameters. The invariants of the left Cauchy-Green tensor can be written in terms of the principal stretches λ_i $(i = 1, 2, 3)$

$$I_1 = \mathrm{tr}\mathbf{B} = \lambda_1^2 + \lambda_2^2 + \lambda_3^2$$
$$I_2 = \frac{1}{2}\left[(\mathrm{tr}\mathbf{B})^2 - \mathrm{tr}(\mathbf{BB})\right] = (\lambda_1\lambda_2)^2 + (\lambda_2\lambda_3)^2 + (\lambda_3\lambda_1)^2$$

From Truesdell and Noll (2004), the Cauchy stress $\mathbf{T}$ can be expressed as

$$\mathbf{T} = -p\mathbf{1} + \mathbf{T}_E \quad (2)$$

$$\mathbf{T}_E = 2\frac{\partial W}{\partial I_1}\mathbf{B} - 2\frac{\partial W}{\partial I_2}\mathbf{B}^{-1} \quad (3)$$

where $\mathbf{1}$ = identity tensor; p = Lagrange multiplier that can be determined from the boundary condition; and the subscript E = extra stress.

From the model structures shown in Fig. 4, the extra stress tensor can be written as the sum of the equilibrium part $\mathbf{T}_E^{(E)}$ and the overstress part $\mathbf{T}_E^{(OE)}$

$$\mathbf{T}_E = \mathbf{T}_E^{(E)} + \mathbf{T}_E^{(OE)} \quad (4)$$

with

$$\mathbf{T}_E^{(E)} = 2\frac{\partial W^{(E)}}{\partial I_{1\mathbf{B}}}\mathbf{B} - \frac{\partial W^{(E)}}{\partial I_{2\mathbf{B}}}\mathbf{B}^{-1} \quad (5)$$

$$\mathbf{T}_E^{(OE)} = 2\frac{\partial W^{(OE)}}{\partial I_{1\mathbf{B}_e}}\mathbf{B}_e - \frac{\partial W^{(OE)}}{\partial I_{2\mathbf{B}_e}}\mathbf{B}_e^{-1} \quad (6)$$

where $\mathbf{B} = \mathbf{F}\mathbf{F}^T$; $\mathbf{B}_e = \mathbf{F}_e\mathbf{F}_e^T$; and $I_{1\mathbf{B}}$ and $I_{2\mathbf{B}}$ = first and second invariants of the left Cauchy-Green tensor $\mathbf{B}$. The subscript e denotes the quantities related to $\mathbf{F}_e$.

Following the concept of Huber and Tsakmakis (2000), the rate of the left Cauchy-Green deformation tensor can be expressed as

$$\dot{\mathbf{B}}_e = \mathbf{B}_e\mathbf{L}^T + \mathbf{L}\mathbf{B}_e - \frac{2}{\eta}\mathbf{B}_e\left(\hat{\mathbf{P}}_E - \hat{\mathbf{P}}_E^{(E)}\right) \quad (7)$$

The superimposed dot indicates the material time derivative; η = viscosity function; $\mathbf{P}_E$ = Mandel stress tensor; and $\mathbf{L}$ = velocity gradient expressed as

$$\mathbf{L} = \dot{\mathbf{F}}\mathbf{F}^{-1} \quad (8)$$

Evolution of Nonlinear Viscosity

Amin et al. (2006b) followed the general constitutive theory based on Huber and Tsakmakis (2000) to propose an explicit description of the evolution equation of nonlinear viscosity by analyzing the experimental data in compression and shear regimes. Eq. (9) represents the constitutive equation of viscosity of the power law type (Amin et al. 2006b) in a general three-dimensional (3D) form

$$\hat{\mathbf{D}}_i = \frac{\left\|\hat{\mathbf{P}}_E^{(OE)}\right\|^{\delta}}{\eta_0\pi^{\delta}\|\mathbf{B}\|^{\varphi}}\hat{\mathbf{P}}_E^{(OE)} \quad (9)$$

where φ, δ, and η_0 = material parameters to be determined; and $\|\boldsymbol{\omega}\| = \sqrt{\boldsymbol{\omega}\cdot\boldsymbol{\omega}}$ = magnitude of a tensor, $\boldsymbol{\omega}$, where $\boldsymbol{\omega}$ = an example tensor quantity. The closed form of the evolution equation of the constitutive equation of nonlinear viscosity can be obtained from Eq. (9)

$$\frac{1}{\eta\left(\hat{\mathbf{P}}_E^{(OE)}, \mathbf{B}\right)} = \frac{1}{\eta_0}\left(\frac{\left\|\hat{\mathbf{P}}_E^{(OE)}\right\|}{\pi}\right)^{\delta}\|\mathbf{B}\|^{-\varphi} \quad (10)$$

In Eqs. (9) and (10), the constant $\pi = (1\ \mathrm{MPa})$ was introduced for dimensional reasons.

Computational Strategy for Viscosity Effect

In analyzing rubber bearings and expansion joints, uniaxial compression and simple shear are the relevant deformation modes to consider. The first-order differential equation presented in Eqs. (7) and (10) for the nonlinear evolution of viscosity was decomposed into a one-dimensional form, as discussed in the next two subsections. A standard numerical method was applied to solve the one-dimensional rate equations. The approach is novel for its inherent simplicity but possesses a limitation in solving a problem for arbitrary or unknown deformation modes (Bhuiyan et al. 2007; Hossain 2007).

Uniaxial Compression Loading

Assuming rubber to be an incompressible material, the total deformation gradient tensor can be written as

$$\mathbf{F} = \begin{bmatrix} \lambda & 0 & 0 \\ 0 & \frac{1}{\sqrt{\lambda}} & 0 \\ 0 & 0 & \frac{1}{\sqrt{\lambda}} \end{bmatrix} \quad (11)$$

Thus, the left Cauchy-Green strain deformation tensor can be evaluated as

$$\mathbf{B} = \mathbf{F}\mathbf{F}^T = \begin{bmatrix} \lambda^2 & 0 & 0 \\ 0 & \dfrac{1}{\lambda} & 0 \\ 0 & 0 & \dfrac{1}{\lambda} \end{bmatrix} \tag{12}$$

Table 1. Elasticity Parameters

Responses	C_2 (MPa)	C_3 (MPa)	C_4 (MPa)	C_5 (MPa)	M	N
Equilibrium	0.145	1.182	−5.297	4.262	0.06	0.27
Instantaneous	0.166	2.477	−11.689	9.707	0.06	0.27
Overstress	0.021	1.295	−6.392	5.445		

Table 2. Viscosity Parameters

Parameter	Value
η_0 (MPa)	1.63
δ	1.46
φ	2.29

Similarly, for the intermediate spring as shown in Fig. 4, one obtains

$$\mathbf{F}_e = \begin{bmatrix} \lambda_e & 0 & 0 \\ 0 & \dfrac{1}{\sqrt{\lambda_e}} & 0 \\ 0 & 0 & \dfrac{1}{\sqrt{\lambda_e}} \end{bmatrix} \quad \text{and} \quad \mathbf{B}_e = \mathbf{F}_e\mathbf{F}_e^T = \begin{bmatrix} \lambda_e^2 & 0 & 0 \\ 0 & \dfrac{1}{\lambda_e} & 0 \\ 0 & 0 & \dfrac{1}{\lambda_e} \end{bmatrix} \tag{13}$$

The rate of deformation gradient tensor is given as

$$\mathbf{L} = \dot{\mathbf{F}}\mathbf{F}^{-1} = \dot{\lambda} \begin{bmatrix} \dfrac{1}{\lambda} & 0 & 0 \\ 0 & -\dfrac{1}{2\lambda} & 0 \\ 0 & 0 & -\dfrac{1}{2\lambda} \end{bmatrix} \quad \text{and}$$
$$\dot{\mathbf{B}}_e = \dot{\lambda}_e \begin{bmatrix} 2\lambda_e & 0 & 0 \\ 0 & -\dfrac{1}{\lambda_e^2} & 0 \\ 0 & 0 & -\dfrac{1}{\lambda_e^2} \end{bmatrix} \tag{14}$$

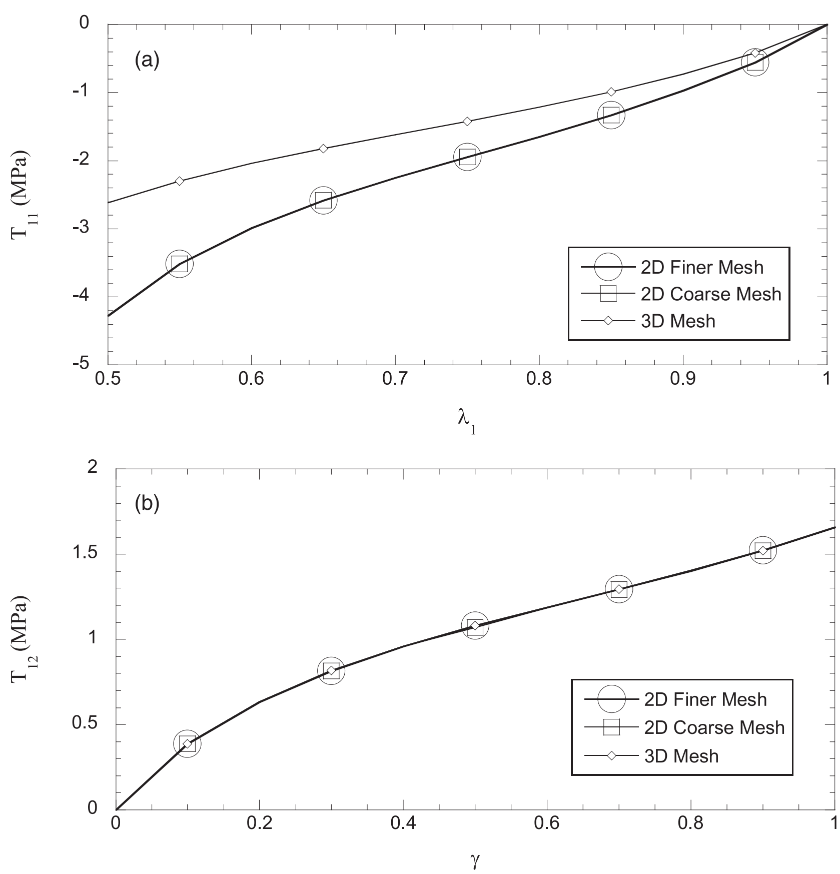

Fig. 5. Effect of 1-direction mesh refinement on stress response in Mesh 3: (a) effect on T_{11} stress; (b) effect on T_{12} stress; 2D coarse mesh: a single rubber layer [l_a : 240 mm, $h(=t_r)$: 5 mm, shape factor 12, Table 3] is divided into 24 elements in 2-direction and one element in 1-direction; 2D fine mesh: a single rubber layer [l_a : 240 mm, $h(=t_r)$: 5 mm, shape factor 12, Table 3] is divided into 24 elements in 2-direction and five elements in 1-direction; 3D mesh: a single rubber layer [l_a : 240 mm, l_b : 240 mm, $h(=t_r)$: 5 mm, shape factor 12, Table 3] is divided into 24 elements in 2-direction and 3-direction and one element in 1-direction; shape factor = $l_a l_b / 2t_r(l_a + l_b)$

Eq. (7) yields

$$\mathbf{B}_e\mathbf{L}^T = \mathbf{B}_e\mathbf{L} = \dot{\lambda}\begin{bmatrix} \frac{\lambda_e^2}{\lambda} & 0 & 0 \\ 0 & -\frac{1}{2\lambda\lambda_e} & 0 \\ 0 & 0 & -\frac{1}{2\lambda\lambda_e} \end{bmatrix} \quad \text{and}$$

$$\left(\mathbf{T} - \mathbf{T}^{(E)}\right)^D = \begin{bmatrix} T_{11}^{(OE)} & 0 & 0 \\ 0 & T_{22}^{(OE)} & 0 \\ 0 & 0 & T_{33}^{(OE)} \end{bmatrix}^D \tag{15}$$

Table 3. Geometry of Rubber Bearings with Different Shape Factors

Shape factor	a (mm)	B (mm)	t_s (mm)	t_r (mm)	n_r	n_s
6	240	240	2	10	6	5
12	240	240	2	5	6	5
15	240	240	2	4	6	5
24	240	240	2	2.5	6	5
30	240	240	2	2	6	5

Now, substituting Eqs. (14) and (15) into Eq. (7) yields

$$\dot{\lambda}_e\begin{bmatrix} 2\lambda_e & 0 & 0 \\ 0 & -\frac{1}{\lambda_e^2} & 0 \\ 0 & 0 & -\frac{1}{\lambda_e^2} \end{bmatrix} = \dot{\lambda}\begin{bmatrix} \frac{\lambda_e^2}{\lambda} & 0 & 0 \\ 0 & -\frac{1}{2\lambda\lambda_e} & 0 \\ 0 & 0 & -\frac{1}{2\lambda\lambda_e} \end{bmatrix}$$

$$+ \dot{\lambda}\begin{bmatrix} \frac{\lambda_e^2}{\lambda} & 0 & 0 \\ 0 & -\frac{1}{2\lambda\lambda_e} & 0 \\ 0 & 0 & -\frac{1}{2\lambda\lambda_e} \end{bmatrix} - \frac{2}{\eta_0}\left(\frac{\left\|\mathbf{T}^{(OE)}\right\|}{\pi}\right)^{\delta}\|\mathbf{B}\|^{-\varphi}$$

$$\times \begin{bmatrix} \lambda_e^2 & 0 & 0 \\ 0 & \frac{1}{\lambda_e} & 0 \\ 0 & 0 & \frac{1}{\lambda_e} \end{bmatrix}\begin{bmatrix} \mathbf{T}_{11}^{(OE)} & 0 & 0 \\ 0 & \mathbf{T}_{11}^{(OE)} & 0 \\ 0 & 0 & \mathbf{T}_{11}^{(OE)} \end{bmatrix}^D \tag{16}$$

Considering the first normal term that corresponds to the loading condition and viscosity at each strain level constant, the relevant rate equation is isolated as

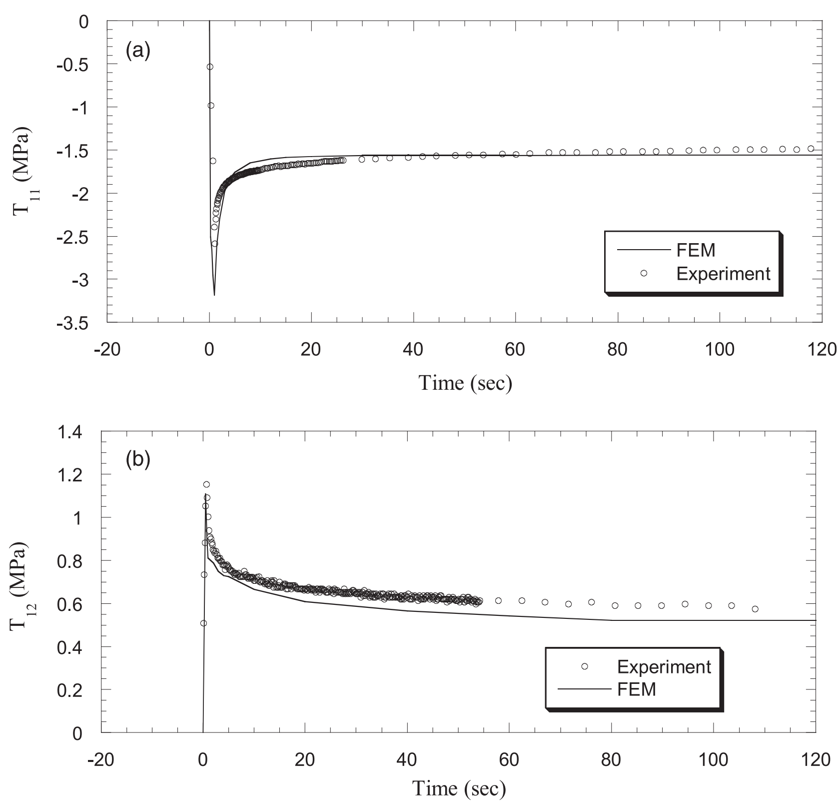

Fig. 6. Numerical simulation of stress relaxation phenomena of high damping rubber under compression and shear: (a) at $\lambda_1 = 0.5$ for Mesh 1; (b) at $\gamma = 1.00$ for Mesh 2 (Fig. 1)

$$2\dot{\lambda}_e\lambda_e = 2\,\frac{\dot{\lambda}}{\lambda}\lambda_e^2 - \frac{4}{3}T_{11}^{(OE)}\lambda_e^2\frac{1}{\eta_0}\left(\frac{\left|T^{(OE)}\right|}{\pi}\right)^{\delta}|\lambda|^{-2\varphi} \tag{17}$$

$$\dot{\lambda}_e = 2\,\frac{\dot{\lambda}}{\lambda}\,\lambda_e - \frac{2}{3}T_{11}^{(OE)}\lambda_e\frac{1}{\eta_0}\left(\frac{\left|T^{(OE)}\right|}{\pi}\right)^{\delta}|\lambda|^{-2\varphi} \tag{18}$$

Eq. (18) is solved by a standard numerical method with adequate solution steps.

Simple Shear Loading

The total deformation gradient and the left Cauchy-Green tensor are given by the following expressions:

$$\mathbf{F} = \begin{bmatrix} 1 & \gamma & 0 \\ 0 & 1 & 0 \\ 0 & 0 & 1 \end{bmatrix} \quad \text{and} \quad \mathbf{B} = \mathbf{F}\mathbf{F}^T = \begin{bmatrix} 1+\gamma^2 & \gamma & 0 \\ \gamma & 1 & 0 \\ 0 & 0 & 1 \end{bmatrix} \tag{19}$$

Similarly, for intermediate spring, these two quantities can be written as

$$\mathbf{F}_e = \begin{bmatrix} 1 & \gamma_e & 0 \\ 0 & 1 & 0 \\ 0 & 0 & 1 \end{bmatrix} \quad \text{and} \quad \mathbf{B}_e = \mathbf{F}_e\mathbf{F}_e^T = \begin{bmatrix} 1+\gamma_e^2 & \gamma_e & 0 \\ \gamma_e & 1 & 0 \\ 0 & 0 & 1 \end{bmatrix} \tag{20}$$

The velocity gradient and the rate of the elastic left Cauchy-Green tensor read as

$$\mathbf{L} = \dot{\mathbf{F}}\mathbf{F}^{-1} = \begin{bmatrix} 0 & \dot{\gamma} & 0 \\ 0 & 0 & 0 \\ 0 & 0 & 0 \end{bmatrix} \quad \text{and} \quad \dot{\mathbf{B}}_e = \begin{bmatrix} 2\gamma_e\dot{\gamma}_e & \dot{\gamma}_e & 0 \\ \dot{\gamma}_e & 0 & 0 \\ 0 & 0 & 0 \end{bmatrix} \tag{21}$$

Using Eq. (17), Eq. (6) yields

$$\mathbf{B}_e\mathbf{L}^T = \begin{bmatrix} \gamma_e\dot{\gamma} & 0 & 0 \\ \dot{\gamma} & 0 & 0 \\ 0 & 0 & 0 \end{bmatrix} \quad \text{and} \quad \mathbf{L}\mathbf{B}_e^T = \begin{bmatrix} \gamma_e\dot{\gamma} & \dot{\gamma} & 0 \\ 0 & 0 & 0 \\ 0 & 0 & 0 \end{bmatrix} \tag{22}$$

$$\left(\mathbf{T} - \mathbf{T}^{(E)}\right)^D = \begin{bmatrix} T_{11}^{(OE)} & T_{12}^{(OE)} & 0 \\ T_{21}^{(OE)} & T_{22}^{(OE)} & 0 \\ 0 & 0 & T_{33}^{(OE)} \end{bmatrix}^D \tag{23}$$

Now, substituting Eqs. (21) and (22) into Eq. (7) yields

$$\begin{bmatrix} 2\gamma_e\dot{\gamma}_e & \dot{\gamma}_e & 0 \\ \dot{\gamma}_e & 0 & 0 \\ 0 & 0 & 0 \end{bmatrix} = \begin{bmatrix} \gamma_e\dot{\gamma} & 0 & 0 \\ \dot{\gamma} & 0 & 0 \\ 0 & 0 & 0 \end{bmatrix} + \begin{bmatrix} \gamma_e\dot{\gamma} & \dot{\gamma} & 0 \\ 0 & 0 & 0 \\ 0 & 0 & 0 \end{bmatrix} - \frac{2}{\eta_0}\left(\frac{\left\|\mathbf{T}^{(OE)}\right\|}{\pi}\right)^{\delta}\|\mathbf{B}\|^{-\phi}\begin{bmatrix} 1+\gamma_e^2 & \gamma_e & 0 \\ \gamma_e & 1 & 0 \\ 0 & 0 & 1 \end{bmatrix} \times \begin{bmatrix} T_{11}^{(OE)} & T_{12}^{(OE)} & 0 \\ T_{21}^{(OE)} & T_{22}^{(OE)} & 0 \\ 0 & 0 & T_{33}^{(OE)} \end{bmatrix}^D \tag{24}$$

Considering the off-diagonal terms that correspond to the simple shear loading condition, the relevant rate equation is isolated as

$$\dot{\gamma}_e = \dot{\gamma} - \frac{4}{3}\,\frac{\gamma_e}{\eta_0}T_{12}^{(OE)}\left(\frac{\left|P_{12}^{(OE)}\right|}{\pi}\right)^{\delta}|\gamma|^{-2\phi} \tag{25}$$

In this context, the effects of the normal components of Eq. (24) are ignored to avoid complexity. This simplification also conforms to

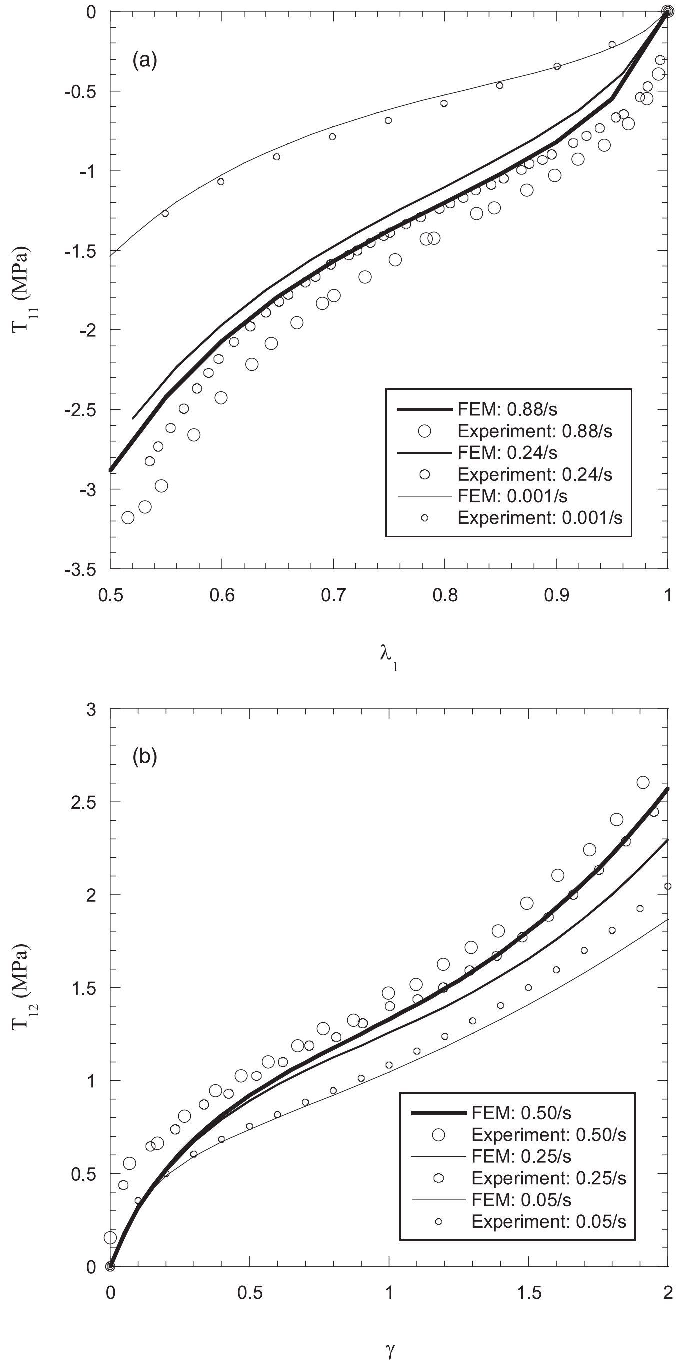

Fig. 7. Simulation of strain-rate dependency effects on rubber blocks, and comparison with experiments in high damping rubber: (a) simulation of monotonic compression experiments at different strain-rates using Mesh 1; (b) simulation of simple shear experiments at different strain-rates using Mesh 2

the experimental conditions (e.g., simple shear). Eq. (25) is solved by a standard numerical method with adequate solution steps.

Material Parameters

Eq. (1) contains the material parameters C_2, C_3, C_4, C_5, M, and N to represent the strain energy density function for the elasticity response; Eq. (10) includes the constants φ, δ, and η_0, which belong to the nonlinear viscosity function. Tables 1 and 2 present the numerical values of the material parameters for high-damping rubber. To identify the parameters (C_2, C_3, C_4, C_5, M, and N) of the hyperelasticity model [Eq. (1)], the experimental data obtained in the compression and shear regime were used, along with a scheme involving the least-squares method to minimize the residuals (Amin et al. 2006a). The viscosity parameters were determined by applying the least-squares method on the $\hat{\mathbf{D}}_i$ versus $\hat{\mathbf{P}}_E^{(OE)} \Big/ \hat{P}_E^{(OE)}\Big|_{\max}$ relationship and the $\|\mathbf{B}\|$ versus $\hat{P}_E^{(OE)}\Big|_{\max}$ relationship so that Eq. (9) is satisfied, where $\hat{P}_E^{(OE)}\Big|_{\max}$ is the past maximum overstress that existed just at the very beginning of the relaxation process, and $\|\mathbf{B}\|$ is the magnitude of the current deformation. For details, please refer to Amin et al. (2006b).

Model Verification

The solution strategy to compute the evolution in Eq. (7) as described in an earlier section was incorporated into a versatile FE program, *FEAP* (Taylor 2006). Three-dimensional (3D) FE analysis was carried out using the FE models of the specimens as shown in Figs. 1(a and b) for compression and simple shear, respectively. Simulation results were checked with experiments to verify the numerical accuracy. To check the effect of the mesh size on the results, a mesh sensitivity analysis was carried out. The 3D models were also reduced to two dimensions for comparison. An eight-node brick element was used to model the rubber and steel. Both the geometric and the material nonlinearities of the rubber layers were considered in the analysis. Steel was considered to be linearly elastic.

Mesh Sensitivity

The convergence of the FE mesh with the smaller mesh size is verified in Fig. 5. The comparison of responses in Fig. 5(a) for uniaxial compression show the inadequacy of a two-dimensional (2D) mesh in the simulation, whereas a 3D mesh with 24 elements was found to be reasonable. In Fig. 5(b), the simple shear case is presented. A 2D coarse mesh with 24 elements in one direction was found to be sufficient for the tested shape factor. A mesh sensitivity test was conducted on a single-layer rubber sheet having a shape factor of 12 and the dimensions given in Table 3 and Fig. 5. Here, the shape factor is defined as

$$\text{Shape factor} = l_a l_b / 2t_r(l_a + l_b) \tag{26}$$

where $l_a l_b$ = loaded area of the bearing; and $2t_r(l_a + l_b)$ = load-free area of the bearing (Fig. 1).

Verification with Experiments

The adequacy of the proposed computational strategy and the FE code hence prepared were verified by comparing the simulation results obtained using the converged mesh size with the results from SR tests. In a SR test, a rubber specimen maintains a desired level of strain at a constant strain rate, and the stress required to maintain this strain is measured for the requisite period of time (relaxation time). The maximum stress occurs when the deformation takes place, and the stress decreases gradually with time from the maximum value. A stretch rate of $0.5/\mathrm{s}$ followed by a relaxation time of 10 min with a stretch level of 0.5 was used in the uniaxial compression mode of the SR tests; however, the shear strain rate of $0.5/\mathrm{s}$ was followed by 10 min with a constant strain level of 2.50 for the simple shear mode in the SR tests (Amin et al. 2002, 2006b).

Fig. 6(a) presents the comparison for uniaxial compression, and Fig. 6(b) the same for the simple shear case. A series of monotonic compression tests at different constant stretch rates up to a 0.5 stretch level was carried out. Constant stretch-rate cases within the range of $0.001-0.96/\mathrm{s}$ were considered in the test. The simple shear tests were carried out in a fashion similar to that of the uniaxial compression tests; however, the shear strain rates were within the range

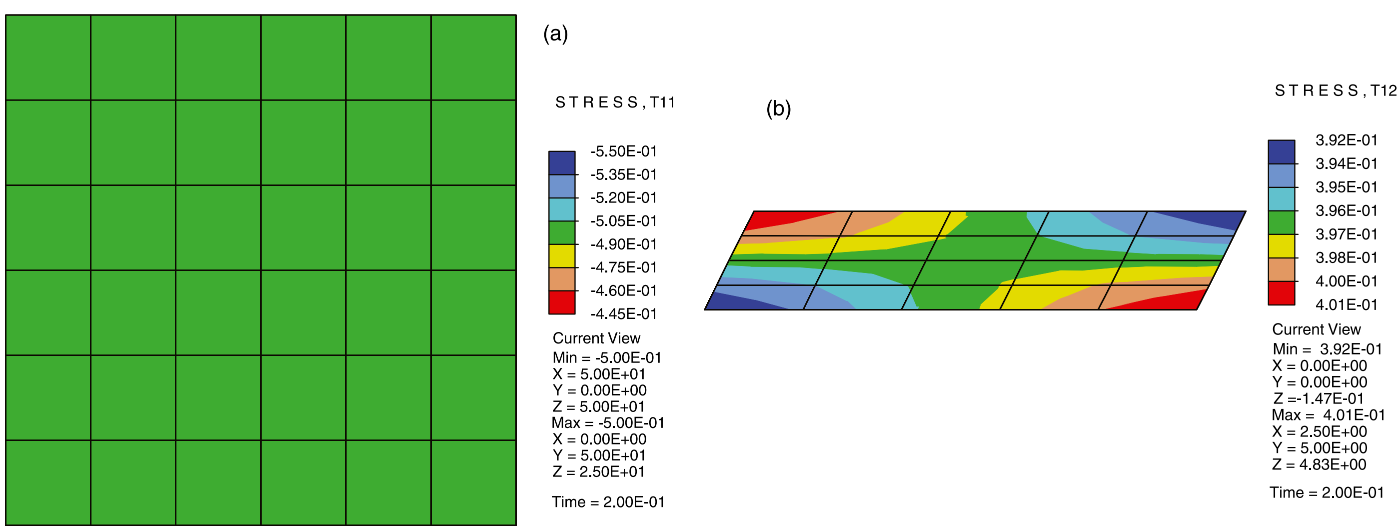

Fig. 8. (Color) Numerical simulation of stress response obtained from high damping rubber: (a) stress contours obtained using Mesh 1 under uniaxial homogeneous compression, $\lambda_1 = 0.9$, $\dot{\lambda} = 0.001/\mathrm{s}$; (b) stress contours obtained using Mesh 2 under simple shear, $\gamma = 0.20$, $\dot{\gamma} = 0.05/\mathrm{s}$ (stress is in megapascals)

of 0.05−0.5/s and the shear strain was increased to 2.50 (Amin et al. 2002, 2006b). The agreement between the experiment and the simulation during the long-term stress relaxation was excellent. The simulation performance in between the instantaneous and the equilibrium states, especially in the first 20 s of the SR history as presented here, seems to be distinctly improved compared with that presented in Hasanpour and Ziaei-Rad (2008) for their data. The simulation of monotonic compression and simple shear experiments are compared with experiments, as shown in Fig. 7. The correlation between the simulation and the experimental results is apparent for the investigated strain-rate cases. At a slower strain rate, the simulation results have a better conformity with those of the experiments, but at a faster strain rate, they do not agree so well. Fig. 8 presents the stress contour for the two deformation cases. The homogeneous deformations both in uniaxial compression and in simple shear modes are obtained from simulation. The observation conforms directly to the experimental boundary condition.

Finally, the simulation of shear stress-strain response obtained from a prototype bearing with a shape factor of 12 was compared with experiments, as shown in Fig. 9. The comparison was independent of its kind as long as the test data points presented in Fig. 9 were not used for identifying the parameters (Tables 1 and 2). Nevertheless, an excellent correlation between the simulation and the experiments is clearly visible. The respective contours for displacement and shear stress are presented in Fig. 10. The contours are reasonably converging, informative, and also indicate the regions where large displacement and stress concentration have taken place.

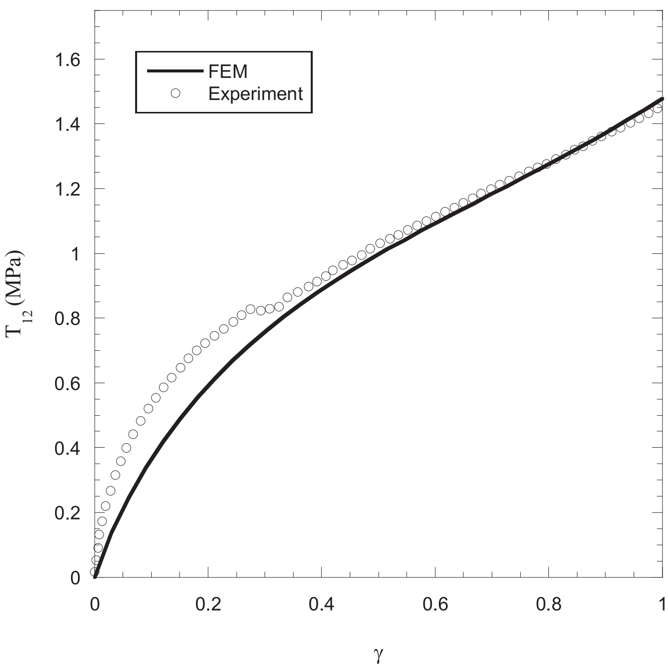

Fig. 9. Comparison of simulation results with experiments obtained in a high damping rubber bearing (data from Bhuiyan et al. 2009); bearing dimension: $l_a: 240$ mm, $l_b: 240$ mm, $t_r: 5$ mm, $t_s: 2.3$ mm, $n_r: 6$, $n_s: 5$, $h: 40$ mm, shape factor 12; applied strain rate, $\dot{\gamma} = 1.5/\mathrm{s}$; Mesh 3 with 92 elements was used in simulation; shape factor $= l_a l_b / 2t_r(l_a + l_b)$

Numerical Experiments

The verification results presented in the preceding sections offer reasonable confidence in conducting numerical experiments within the scope of the proposed strategy. In this context, this section provides information about the shape factor effect of bearing on a stress field in a steel plate laminated rubber expansion joint.

Shape Factor Effect in Laminated Rubber Bearings

Fig. 11 presents the shear responses of the bearing obtained from bearings with different shape factors (Table 3). The trend of an increase in response for the bearings with a large shape factor is noticeable in the figure. For large shape factors, the shear stiffness of the bearing increases at a nonproportional rate. Furthermore, in addition to the nonlinearity in the response at low, moderate, and large strain levels depicted by the hyperelasticity relation [Eq. (1)], the influence of viscosity on the system's response is also perceivable. All this information supplements the work of Imbimbo and De Luca (1998) for uniaxial compression and Matsuda (2004) for shear deformation.

Steel Plate Laminated Rubber Expansion Joints

Figs. 2 and 3 present the as-built basic geometry of a steel plate laminated rubber expansion joint used in a bridge in Bangladesh. Replacement of such joints on the bridge deck requires the bridge to close and is therefore considered to be a major repair work. The

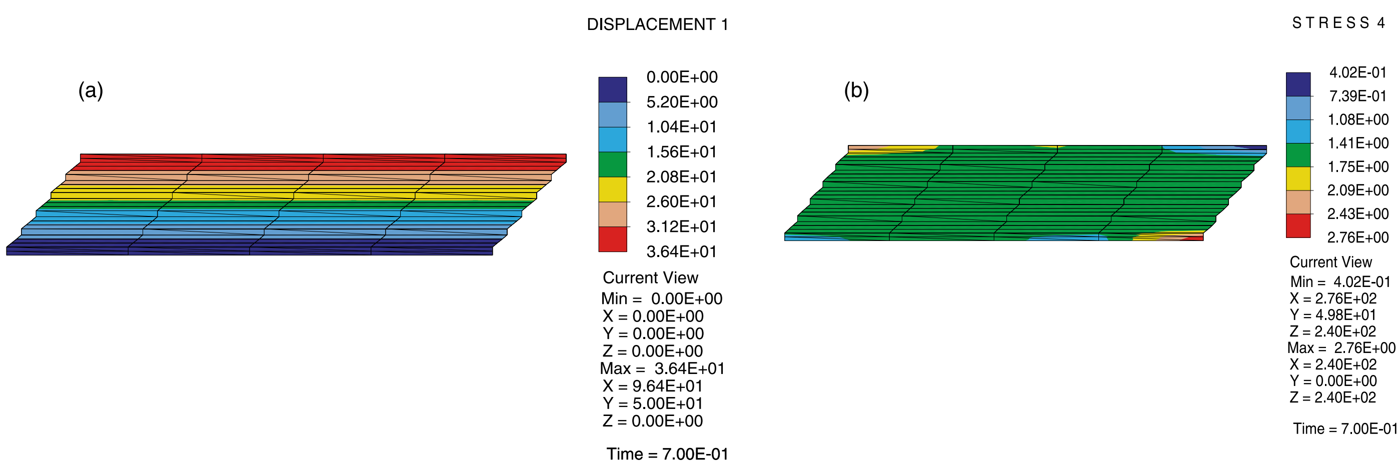

Fig. 10. (Color) Numerical simulation of stress response obtained from high damping rubber bearing (Fig. 6): (a) displacement contours and (b) stress contours at $\gamma = 0.20$, $\dot{\gamma} = 0.75/\mathrm{s}$ (stress is in megapascals); Mesh 3 with 92 elements was used in simulation

separation of the bottom layer of rubber from the steel plate is found to initiate the damage of the expansion joints. Fig. 12 presents the indicative interfacial stress field of such a typical expansion joint obtained using the simulation results. The high-stress-concentration regions located around the steel plate boundaries are shown as stress contours. The 3D solid elements are used to model the rubber and steel layers. A loading configuration combined with compression and shear loadings is used in the FE simulation. However, to remain in line with the leading objective of this essay, further complexities associated with truly understanding and modeling the interface phenomenon between rubber and steel in detail were avoided. Instead, an absolute bonding between the rubber and steel plate was assumed. Such a simplification may weaken the precise assessment of stresses in stress concentration zones because additional effects in the FE model (e.g., frictional slip, shear, adhesion, elastic mismatch, and so forth) that may act in those zones are ignored. Yet the resulting qualitative high stress concentration regions located around the interface of the rubber and steel layers as obtained from the performed simulation closely conform to the line of failures observed in the field.

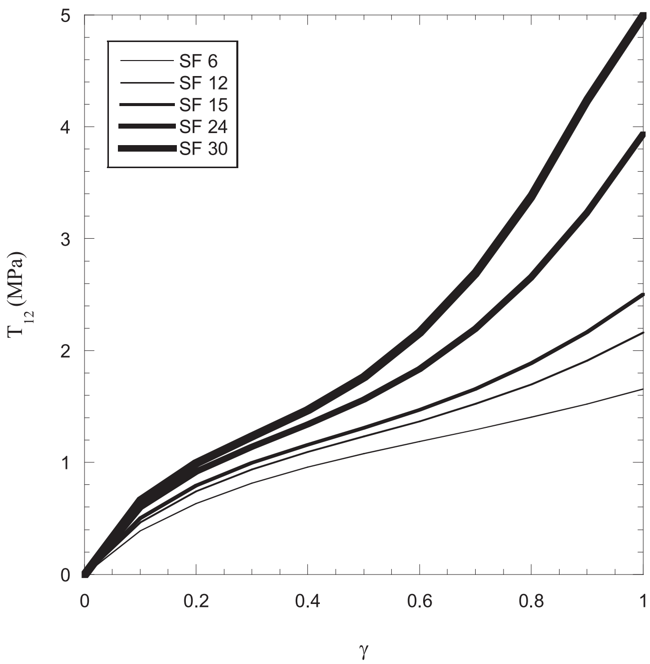

Fig. 11. Effect of shape factor on the shear stress, T_{12}-shear strain, γ response of the bearing

Conclusion

A constitutive model of viscohyperelasticity for rubber was included in a computational strategy to solve boundary value problems under compression and simple shear. The development avoided rigorous mathematical manipulations and therefore seemed suitable for use as a design aid. However, additional attempts were made in the work to reassure the readers of the adequacy of such a simplification in reproducing experimental results from rubber specimens and rubber bearings for the relevant deformation modes. The developed code was used to conduct numerical experiments on rubber bearings with different shape factors and rubber expansion joints. The information obtained regarding this effect conformed to other published results and therefore, is also useful at the design desk.

Acknowledgments

The authors are very grateful to Professor H. Horii, Department of Civil Engineering, University of Tokyo, Japan, for his valuable

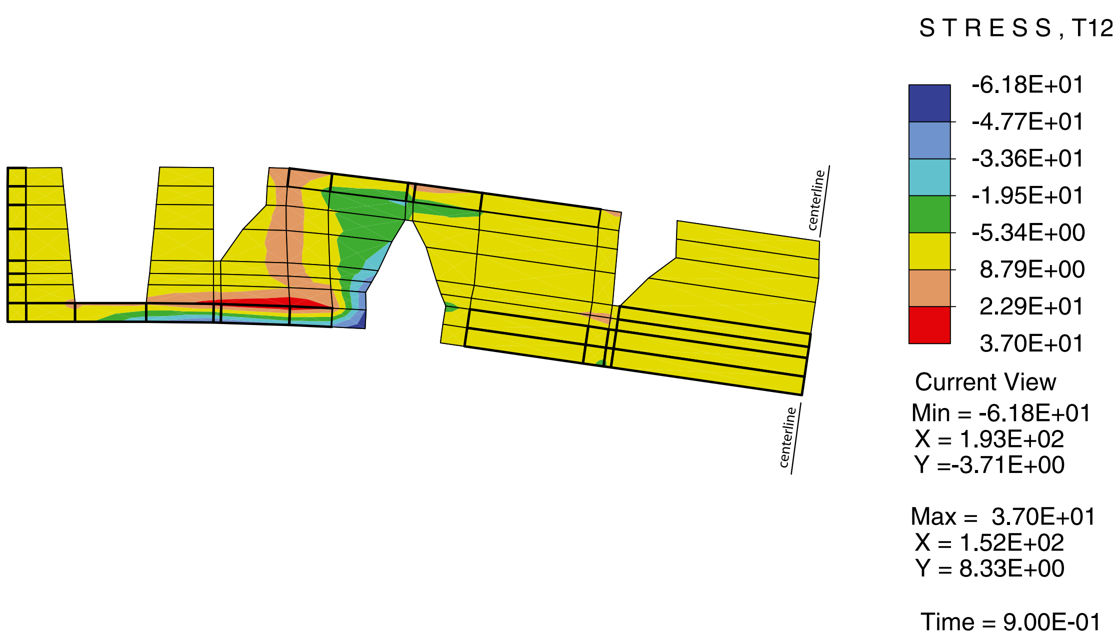

Fig. 12. (Color) T_{12} contour in the expansion joint (Figs. 2 and 3) obtained via FE simulation; the contour is superimposed on the deformed mesh; loading condition: total uniformly distributed load in vertical direction: 150 kN and differential shear strain, $\gamma = 0.05$ applied at a strain rate of $1/s$ between the two ends; the applied shear strain corresponds to the displacement caused by vertical reaction forces; the location of stress concentration is visible; material data follow from Tables 1 and 2 as the exact type of rubber used there, and corresponding material parameters are not available today (stress is in megapascals)

comments and suggestions and particularly for allowing the use of the experimental facilities of his laboratory to carry out the mechanical tests in the investigation. The authors gratefully acknowledge the kind cooperation extended by the Yokohama Rubber Co. in providing test specimens. The authors also sincerely appreciate the funding provided by the Japanese Ministry of Education, Science, Sports and Culture as Grant-in-Aid for Scientific Research (C) (No. 12650457) to carry out this research.

References

Amin, A. F., Wiraguna, S. I., Bhuiyan, A. R., and Okui, Y. (2006a). "Hyperelasticity model for finite element analysis of natural and high damping rubbers in compression and shear." *J. Eng. Mech.*, 10.1061/(ASCE)0733-9399(2006)132:1(54), 54–64.

Amin, A. F. M. S. (2001). "Constitutive modelling for strain-rate dependency of natural and high damping rubbers." Ph.D. thesis, Saitama Univ., Saitama, Japan.

Amin, A. F. M. S., Alam, M. S., and Okui, Y. (2002). "An improved hyperelasticity relation in modeling viscoelasticity response of natural and high damping rubbers in compression: Experiments, parameter identification and numerical verification." *Mech. Mater.*, 34(2), 75–95.

Amin, A. F. M. S., Lion, A., Sekita, S., and Okui, Y. (2006b). "Nonlinear dependence of viscosity in modeling the rate-dependent response of natural and high damping rubbers in compression and shear: Experimental identification and numerical verification." *Int. J. Plast.*, 22(9), 1610–1657.

Bergström, J. S., and Boyce, M. C. (1998). "Constitutive modeling of the large strain time-dependent behavior of elastomers." *J. Mech. Phys. Solids*, 46(5), 931–954.

Bhuiyan, A. R., Amin, A. F. M. S., Hossain, T., and Okui, Y. (2007). "Nonlinear viscosity law for rate-dependent response of high damping rubber: FE implementation and verification." *Proc., 5th European Conf. for Constitutive Models for Rubber*, A. Boukamel, L. Laiarinandrasana, S. Méo, and E. Verron, eds., Taylor & Francis, London, 274–284.

Bhuiyan, A. R., Okui, Y., Mitamura, H., and Imai, T. (2009). "A rheology model of high damping rubber bearings for seismic analysis: Identification of nonlinear viscosity." *Int. J. Solids Struct.*, 46(7–8), 1778–1792.

Dal, H., and Kaliske, M. (2009). "Bergström–Boyce model for nonlinear finite rubber viscoelasticity: Theoretical aspects and algorithmic treatment for the FE method." *Comput. Mech.*, 44(6), 809–823.

FEAP 8.1 [Computer software]. Berkeley, CA, Dept. of Civil and Environmental Engineering, Univ. of California at Berkeley.

Hasanpour, K., and Ziaei-Rad, S. (2008). "Finite element simulation of polymer behaviour using a three-dimensional, finite deformation constitutive model." *Comput. Struct.*, 86(15–16), 1643–1655.

Hasanpour, K., Ziaei-Rad, S., and Mahzoon, M. (2009). "A large deformation framework for compressible viscoelastic materials: Constitutive equations and finite element implementation." *Int. J. Plast.*, 25(6), 1154–1176.

Haupt, P., and Sedlan, K. (2001). "Viscoplasticity of elastomeric materials: Experimental facts and constitutive modelling." *Arch. Appl. Mech.*, 71(2–3), 89–109.

Hossain, T. (2007). "Finite element formulation and modelling of rate dependent response of natural and high damping rubbers." M.Sc. Eng. thesis, Dept. of Civil Engineering, Bangladesh Univ. of Engineering and Technology, Dhaka, Bangladesh.

Huber, N., and Tsakmakis, C. (2000). "Finite deformation viscoelasticity laws." *Mech. Mater.*, 32(1), 1–18.

Imbimbo, M., and De Luca, A. (1998). "F.E. stress analysis of rubber bearings under axial loads." *Comput. Struct.*, 68(1–3), 31–39.

Johlitz, M., Diebels, S., Batal, J., Steeb, H., and Possart, W. (2008). "Size effects in polyurethane bonds: Experiments, modelling and parameter identification." *J. Mater. Sci.*, 43(14), 4768–4779.

Johlitz, M., Steeb, H., Diebels, S., Chatzouridou, A., Batal, J., and Possart, W. (2007). "Experimental and theoretical investigation of nonlinear viscoelastic polyurethane systems." *J. Mater. Sci.*, 42(23), 9894–9904.

Kelly, J. M. (1997). *Earthquake resistant design with rubber*, Springer, London.

Lion, A. (1996). "A constitutive model for carbon black filled rubber: Experimental investigations and mathematical representation." *Contin. Mech. Thermodyn.*, 8(3), 153–169.

Lubliner, J. (1973). "On the structure of the rate equations of materials with internal variables." *Acta Mech.*, 17(1–2), 109–119.

Lubliner, J. (1985). "A model for rubber viscoelasticity." *Mech. Res. Commun.*, 12(2), 93–99.

Matsuda, A. (2004). "Evaluation for mechanical properties of laminated rubber bearings using finite element analysis." *J. Pressure Vessel Technol.*, 126(1), 134–140.

Miehe, C., and Keck, J. (2000). "Superimposed finite elastic-viscoelastic-plastoelastic stress response with damage in filled rubbery polymers. Experiments, modelling and algorithmic implementation." *J. Mech. Phys. Solids*, 48(2), 323–365.

Mooney, M. (1940). "A theory of large elastic deformation." *J. Appl. Phys.*, 11(9), 582–592.

Rivlin, R. S., and Saunders, D. W. (1951). "Large elastic deformations of isotropic materials. VII. Experiments on the deformation of rubber." *Phil. Trans. R. Soc. London, Ser. A*, 243(865), 251–288.

Shariff, M. H. B. M. (2000). "Strain energy function for filled and unfilled rubberlike material." *Rubber Chem. Technol.*, 73(1), 1–18.

Simo, J. C. (1987). "On a fully three-dimensional finite-strain viscoelastic damage model: Formulation and computational aspects." *Comput. Methods Appl. Mech. Eng.*, 60(2), 153–173.

Simo, J. C., and Taylor, R. L. (1991). "Quasi-incompressible finite elasticity in principal stretches. Continuum basis and numerical algorithms." *Comput. Methods Appl. Mech. Eng.*, 85(3), 273–310.

Simo, J. C., Taylor, R. L., and Pister, K. S. (1985). "Variational and projection methods for the volume constraint in finite deformation elasto-plasticity." *Comput. Methods Appl. Mech. Eng.*, 51(1–3), 177–208.

Spathis, G., and Kontou, E. (2008). "Modeling of nonlinear viscoelasticity at large deformations." *J. Mater. Sci.*, 43(6), 2046–2052.

Spuler, T., Moor, G., and Ghosh, C. (2010). "Supporting economical bridge construction—The central hinge bearings of the 2nd Shitalakshya Bridge." *Proc., IABSE-JSCE Joint Conf. on Advances in Bridge Engineering-II*, Amin, Okui, Bhuiyan, eds., International Association for Bridge and Structural Engineering, Zurich, Switzerland/Japan Society of Civil Engineers, Tokyo, 275–280.

Taylor, R. L. (2006). *FEAP—A finite element analysis program. User's manual, version 8.1*, Dept. of Civil and Environmental Engineering, Univ. of California, Berkeley, CA.

Treloar, L. R. G. (1944). "Stress-strain data for vulcanized rubber under various types of deformations." *Trans. Faraday Soc.*, 40, 59–70.

Truesdell, C., and Noll, W. (2004). *The non-linear field theories of mechanics*, Springer-Verlag, Berlin.

Zienkiewicz, O. C., and Taylor, R. L. (2006). *The finite element method for solid and structural mechanics*, 6th Ed., Butterworth-Heinemann, Oxford, U.K.